2014

Hubble Space Telescope and Spitzer point-source detection and optical extinction in powerful narrow-line radio galaxies

Monthly Notices of the Royal Astronomical Society, Oxford, v. 439, p. 1270-1285, 2014
http://www.producao.usp.br/handle/BDPI/46261

Monthly Notices
of the
ROYAL ASTRONOMICAL SOCIETY

MNRAS **439,** 1270–1285 (2014)
Advance Access publication 2014 February 7

doi:10.1093/mnras/stt2444

Hubble Space Telescope and *Spitzer* point-source detection and optical extinction in powerful narrow-line radio galaxies

E. A. Ramírez,[1]★ C. N. Tadhunter,[2] D. Dicken,[3] M. Rose,[2] D. Axon,[4,5]† W. Sparks[6] and C. Packham[7]

[1]*Universidade de São Paulo, IAG, Rua do Matão 1226, Cidade Universitária, São Paulo 05508-900, Brazil*
[2]*Department of Physics and Astronomy, University of Sheffield, Sheffield S3 7RH, UK*
[3]*Institut d'Astrophysique Spatiale, CNRS, Université Paris Sud, F-91405 Orsay, France*
[4]*Physics Department, Rochester Institute of Technology, Rochester, NY 14623, USA*
[5]*School of Mathematical and Physical Sciences, University of Sussex, Brighton BN1 9QH, UK*
[6]*Space Telescope Science Institute, 3700 San Martin Drive, Baltimore, MD21218, USA*
[7]*Department of Physics & Astronomy, University of Texas at San Antonio, One UTSA Circle, San Antonio, TX 78249, USA*

Accepted 2013 December 16. Received 2013 November 12; in original form 2013 August 29

ABSTRACT

We present an analysis of infrared *Hubble Space Telescope* (*HST*) and *Spitzer* data for a sample of 13 Fanaroff–Riley II (FRII) radio galaxies at $0.03 < z < 0.11$ that are classified as narrow-line radio galaxies (NLRGs). In the context of unified schemes for active galactic nuclei (AGNs), our direct view of AGNs in NLRGs is impeded by a parsec-scale dusty torus structure. Our high-resolution infrared observations provide new information about the degree of extinction resulting from the torus, and about the incidence of obscured AGNs in NLRGs.

We find that the point-like nucleus detection rate increases from 25 per cent at 1.025 μm, to 80 per cent at 2.05 μm, and to 100 per cent at 8.0 μm. This supports the idea that most NLRG host an obscured AGN in their centre. We estimate the extinction from the obscuring structures using X-ray, near-IR and mid-IR data. We find that the optical extinction derived from the 9.7 μm silicate absorption feature is consistently lower than the extinction derived using other techniques. This discrepancy challenges the assumption that all the mid-infrared emission of NLRG is extinguished by a simple screen of dust at larger radii. This disagreement can be explained in terms of either weakening of the silicate absorption feature by (i) thermal mid-IR emission from the narrow-line region, (ii) non-thermal emission from the base of the radio jets, or (iii) by direct warm dust emission that leaks through a clumpy torus without suffering major attenuation.

Key words: galaxies: active – galaxies: nuclei – infrared: galaxies.

1 INTRODUCTION

Orientation-based unified schemes attempt to explain the various features observed in active galactic nuclei (AGNs) in terms of the way we observe them, rather than in terms of fundamental physical differences between the various types of AGNs (Barthel 1989; Antonucci 1993; Urry & Padovani 1995).

In the standard orientation-based unified scheme, the AGN is surrounded by a dusty obscuring torus, with the torus axis oriented parallel to the radio axis. The high-density broad-line region (BLR) is situated near the nucleus ($r < 1$ pc), and surrounding this is the lower-density narrow-line region (NLR) extending to ∼0.1–1 kpc. In objects oriented face-on, the BLR is directly visible and therefore such objects are classified as type 1 galaxies; type 2 galaxies, on the other hand, are oriented closer to edge-on, with the torus preventing a direct view of their BLR at optical wavelengths.

Clearly, the dusty torus structure is a key element in orientation-based unified schemes for quasars and radio galaxies (Barthel 1989; Urry & Padovani 1995). However, despite the importance of the torus, little is known about its morphology, the extinction it imposes, and its relationship with the kiloparsec-scale dust structure. Attempts to investigate the structure of the torus have been made based on modelling the mid-infrared spectral energy distribution (SED, e.g. Pier & Krolik 1992; Nenkova, Ivezić & Elitzur 2002). Although such studies have provided important results, they probe the characteristics of the torus in an indirect way. Near-infrared (near-IR; 1–3 μm) observations can provide direct information about the inner kiloparsecs of the AGN and the properties of the torus, as such wavelengths can penetrate the dust in the central region of the AGN more easily than optical wavelengths. This is because the extinction is a wavelength-dependent phenomenon: it is much greater

★ E-mail: e.ramirez@usp.br
† Deceased.

at UV wavelengths than at longer IR wavelengths (Draine 1989). Furthermore, because the near-IR emission in AGNs is emitted by the hottest dust located in the inner parts of the torus, such observations can provide an estimate of the total extinction caused by the torus.

The effectiveness of near-IR observations from the ground in tracing the inner parts of AGNs was first demonstrated by Djorgovski et al. (1991), who successfully detected a compact core source in Cygnus A. Unfortunately, the early ground-based observations lacked the spatial resolution required to accurately separate the AGN emission from the starlight of the host galaxy. Now, the *Hubble Space Telescope* (*HST*) now provides unprecedented opportunities to study obscured AGNs with greater resolution and stability at IR wavelengths than is possible with ground-based observations. Moreover, *Spitzer* is orders of magnitude more sensitive than previous satellites working at mid- to far-IR wavelengths (3–24 and 24–160 μm, respectively), and its instruments provide better mid-IR spectroscopy observations than are available from older studies.

Indeed, *HST* studies of two powerful radio galaxies – 3C 405 (Cygnus A) and 3C 433 – have shown unresolved point sources clearly detected at longer near-IR wavelengths (Tadhunter et al. 1999; Ramírez et al. 2009), suggesting a direct detection of the hidden AGN, which is extinguished by foreground dust. However, 3C 405 and 3C 433 may not be typical of the general population of powerful radio galaxies. Therefore it is important to extend such studies to larger, complete samples of radio galaxies, in order to determine the properties of the near-IR core sources in the population as a whole.

In this paper we present near-IR *HST* and mid-IR *Spitzer* observations of a complete sample of 10 nearby powerful radio galaxies. We analyse the unresolved point-source occurrence, and the optical extinction induced by the dusty torus structure in the context of orientation-based unified schemes. The sample, observations and data reduction are described in Section 2. The near- and mid-IR point-source detection rates and fluxes are presented in Section 3. The optical extinctions derived from five techniques are presented in Section 4. Finally, the discussion and the conclusions are given in Sections 5 and 6, respectively. This is the first of two papers. In the second paper, we will describe the polarization properties of the near-IR core sources.

2 OBSERVATIONS

2.1 *HST* sample

The main data set used in this study consists of deep *HST* observations taken with the near-IR camera and multi-object spectrometer (NICMOS), and the main sample comprises all 10 narrow-line radio galaxies (NLRGs) at redshifts $0.03 < z < 0.11$ in the 3CRR catalogue (Laing, Riley & Longair 1983) classified as Fanaroff–Riley II (FRII) sources (Fanaroff & Riley 1974): we term this sample the 'complete sample'. In addition, we analysed archival observations of 3C 293, 3C 305 and 3C 405 (Cygnus A). They are included because these are the only other 3C powerful radio galaxies at similar redshifts observed with *HST*/NICMOS in a similar way to our complete sample (with the polarimeter filters; see Subsection 2.2). These three additional objects along with the 10 objects in the complete sample comprise an 'extended sample' of 13 radio galaxies, all located in the Northern hemisphere. Table 1 presents the properties of the complete sample and the three objects included in the extended *HST*/NICMOS sample.

Table 1. *HST* sample general characteristics. Column (1) source name from the 3CRR catalogue (Laing et al. 1983). (2) Redshifts (Spinrad et al. 1985; Leahy, Bridle & Strom 2000). (3) Radio morphological classification. (3.1) References of the radio morphological classification: (*a*) Fanaroff & Riley (1974); (*b*) Laing et al. (1983); (*c*) Tadhunter (private communication); (*d*) Leahy et al. (2000); (*e*) Carilli & Barthel (1996). (4) The 178-MHz total luminosity ($H_0 = 70\,km\,s^{-1}\,Mpc^{-1}$) taken from: Mullin, Riley & Hardcastle (2008), 3C 33, 3C 98, 3C 192, 3C 236, 3C 285, 3C 321, 3C 433, 3C 452, 4C 73.08; Spinrad et al. (1985), 3C 277.3, 3C 405; Leahy et al. (2000), 3C 293, 3C 305. (5) Optical classification from NED except for 3C 305, 3C 236 and 3C 277.3 (Buttiglione et al. 2009). NLRG, narrow-line radio galaxy; WLRG, weak-line radio galaxy.

		HST sample			
Source	Redshift	Radio	Ref.	$\log_{10}(L_{178})$	Optical
	z	classification		W Hz^{-1} sr^{-1}	classification
(1)	(2)	(3)	(3.1)	(4)	(5)
3C 33	0.0597	FR II	*a*	25.59	NLRG
3C 98	0.0306	FR II	*a*	24.95	NLRG
3C 192	0.0598	FR II	*a*	25.19	NLRG
3C 236	0.1005	FR II	*b*	25.47	WLRG
3C 277.3	0.0850	FR I/FR II	*c*/*a*	25.05	WLRG
3C 285	0.0794	FR II	*a*	25.18	NLRG
3C 321	0.0961	FR II	*b*	25.41	NLRG
3C 433	0.1016	FR II	*c*	26.09	NLRG
3C 452	0.0811	FR II	*a*	25.87	NLRG
4C 73.08	0.0580	FR II	*b*	24.99	NLRG
3C 293	0.0450	FR I/FR II	*c*/*d*	24.77	WLRG
3C 305	0.0416	FR I/FR II	*b*/*c*	24.80	NLRG
3C 405	0.0561	FR II	*e*	27.69	NLRG

2.2 *HST* observations

Dedicated observations of the complete sample were made during Cycle 13, between April 2005 and June 2006 (GO 10410, principal investigator (PI): C. N. Tadhunter). The *HST* observations for this study were obtained using the F110W, F145M and F170M filters (central wavelengths: 1.025, 1.45 and 1.7 μm, respectively), and using the three long polarimeter POL-L filters centred at 2.05 μm. The sources were observed with NICMOS 2 (NIC2) through the F110W and POL-L filters, and with NICMOS 1 (NIC1) through the F145M and F170M filters. NIC1 and NIC2 cameras have fields of view of 11 arcsec× 11 arcsec (0.043 arcsec-sized pixels) and 19.2 arcsec× 19.2 arcsec (0.075 arcsec-sized pixels), respectively. The three polarizer filter images were co-added to form a deep 2.05-μm image, allowing the possibility of penetrating the circumnuclear dust and observing the AGN directly. Note that the polarization analysis for the sources in the sample will be presented in a forthcoming paper. The *HST* provides a theoretical spatial resolution of 0.1, 0.15, 0.18 and 0.21 arcsec at 1.025, 1.45, 1.7 and 2.05 μm, respectively. All the observations were executed in multiple accumulate mode (multiaccum[1]). The observational details for the complete sample, and the three additional sources in the extended sample of 13 sources are presented in Table 2.

For the GO 10410 observations, while NIC2 chopped to the sky, coordinated parallel exposures were made with the NIC1 camera, using the F145M and F170M filters. This ensured that, while the

[1] Multiaccum is a pre-defined sequence of multiple non-destructive readout exposures, used to cope with saturated pixels and cosmic rays, and to increase the dynamic range of the observations; that is, to increase the charge capacity of the pixels.

Table 2. Observation details. *HST* observations details: the column POL-L gives the exposure time for each of the three POL-L filters; '–' indicates data unavailable. Observation details. *Spitzer*–IRAC observation details: PI of program 3418, M.R. Birkinshaw; PI of program 20174, D.E. Harris. Observation details. *Spitzer*–IRS observation details: exposure times are the total integration time on source; that is, integration time times the number of cycles; 's' and 'm' indicate staring- and mapping-mode observations, respectively. The spectra taken in mapping mode had effective integration times on source a factor of 2–34 lower than those for the staring-mode program, leading to, in general, spectra with lower signal-to-noise ratios. PI of program 3624, R. Antonucci; PI of program 20719, S.A. Baum; PI of program 3349, R. Siebenmorgen; PI of program 20525, R. Antonucci; PI of program 82, G. Rieke.

Source	*HST* observation details						*Spitzer*–IRAC observations details			*Spitzer*-IRS observations details.						
	Prog. ID	Filter exp. time (s)				Date	Prog. ID	Date	Exp. time[b] (s)	Prog. ID mode	Date	Exp. time (s)				obs.
		F110W NIC2	F145M NIC1	F170M NIC1	POL-L NIC2							SL2	SL1	LL2	LL1	
3C 33	10410	768	2048	1024	1024	2005-07-10	3418	2005-01-16	160.8	3624	2005-01-11	120	120	240	120	s
3C 98	10410	768	2048	1024	1024	2005-08-28	3418	2005-02-23	160.8	20719	2006-09-06	14	14	14	14	m
3C 192	10410	768	2048	1024	1024	2005-06-15	3418	2004-11-01	160.8	3624	2005-11-19	120	120	240	120	s
3C 236	10410	768	2048	1024	1024	2005-06-15	3418	2004-12-16	160.8	20719	2005-12-12	14	14	14	14	m
3C 277.3	10410	768	2048	1024	1024	2005-08-03	no obs.	–	–	no obs.	–	–	–	–	–	–
3C 285	10410	960	2048	1024	1024	2005-11-21	3418	2004-12-17	160.8	20719	2006-01-17	14	14	14	14	m
3C 321	10410	768	2048	1024	1024	2005-08-22	3418	2005-03-27	160.8	3349	2005-02-07	28	28	30	30	s
3C 433	10410	768[a]	768	768	832	2005-08-22	no obs.	–	–	3624	2005-07-13	120	120	240	120	s
3C 452	10410	960	2048	1024	1024	2006-06-15	3418	2004-11-27	160.8	3624	2004-12-09	120	120	240	120	s
4C 73.08	10410	1536	2048	1024	1024	2005-04-21	3418	2004-12-16	160.8	no obs.	–	–	–	–	–	–
3C 293	7219	480	–	–	–	1998-01-08	3418	2005-06-11	160.8	20525	2006-01-18	480	720	360	240	s
	7853	–	–	–	2176	1998-08-19										
3C 305	7853	–	–	2176	2176	1998-07-19	3418	2004-11-25	160.8	20719	2006-04-26	14	14	14	14	m
3C 405	7258	1536[a]	192	576	2688	1997-12-15	20174	2005-10-21	964.8	82	2004-05-14	28	28	60	60	s

[a] Observed with NIC1. [b] Exposure time on source per IRAC channel.

main NIC2 detector was chopping to the sky, the target was in NIC1 for at least some of the exposures with NIC2. This observation strategy provides bonus observations at 1.45 and 1.7 μm within the granted observation time. The observations of the GO 7258 program (PI: C. Tadhunter; details in Tadhunter et al. 1999 and Tadhunter et al. 2000) were executed in the same fashion.

Although the parallel observation plan has the advantage of increasing observation efficiencies, unfortunately, owing to the use of a chop that was not precisely the same as the spacing between NIC1 and NIC2, the galaxy may be slightly out of the field of view (FoV), especially when the telescope dithers. As a result of this potential difficulty in centring the source, there is only one on-source dither exposure of 3C 405 at 1.45 μm, and at 1.7 μm the galaxy falls at the same position in the FoV. These images are therefore too noisy to be useful. This is not the case, however, for the 1.025- and 2.05-μm observations, which we have used. For 3C 293 and 3C 305 we used archive data from two observation programs: GO 7219 (PI: N. Scoville) and GO 7853 (PI: N. Jackson).

2.3 *HST* data reduction

The *HST* data were passed through the standard NICMOS pipeline calibration software CALNICA (Thatte et al. 2009). The CALNICA task removes instrumental signatures and cosmic ray hits, and combines multiple readouts when the observations were made in multiaccum mode. Subsequently, we further reduced the CALNICA output with IRAF (Image Reduction and Analysis Facility; Tody 1986), median-combining the dithers on the source with IMCOMBINE, and using the same process for the dithers on the sky. The combined sky frame was then subtracted from the combined source frame. Possible remaining hot pixels and detector quadrant features were removed by hand using the CLEAN task in the FIGARO package of the STARLINK software library.

2.4 *Spitzer* observations

We also obtained Infrared Array Camera (IRAC) and Infrared Spectrograph (IRS) data for the sample objects from the public *Spitzer* archive. These data, together with the *HST* observations, enable the complete near- to mid-IR SEDs to be determined, allowing a more detailed investigation of the objects. The lower extinction at mid-IR wavelengths potentially allows even less obscured views of the inner regions of AGNs than are possible at near-IR wavelengths. Analysis of the mid-IR AGN emission can also provide another indicator of the AGN detection rate and of the extinction of dust, based on the mid-IR SED and of the silicate absorption feature, respectively.

2.4.1 *IRAC data*

We used all four mid-IR wavelength bands observed by IRAC: 3.6, 4.5, 5.8 and 8.0 μm. The theoretical spatial resolution achieved by *Spitzer* at 3.6, 4.6, 5.8 and 8.0μm is 1.1, 1.3, 1.7 and 2.4 arcsec, respectively – much lower than the resolution achieved by the *HST* (∼0.2 arcsec at 2.05 μm). The FoV covered by all four channels is 5.2 arcmin × 5.2 arcmin in 256 × 256 pixels, giving a pixel scale of 1.2 arcsec per pixel. Unfortunately, there are no IRAC data available for 3C 277.3 and 3C 433 (see Table 2). For these two sources we used Wide-field Infrared Survey Explorer (WISE; Wright et al. 2010) photometric measurements (see Subsection 3.2 for details).

We downloaded the post-basic calibrated data (post-BCD) (version S18.7.0) products for all sources and carried out the photometric measurements. The BCD pipeline executes: (1) correction of instrumental signatures, (2) dark current subtraction, (3) sky background subtraction from a pre-selected region of low zodiacal background, (4) flat-field correction, (5) the flagging of possible cosmic rays hits, and (6) flux calibration. Consecutively, the post-BCD pipeline refines the telescope pointing, attempts to correct for

residual bias variations, and produces mosaicked images. The total exposure times for the images are indicated in Table 2.

2.4.2 *IRS data*

IRS spectroscopic data were obtained to measure the silicate 9.7-μm absorption feature. The observations were obtained using the low-resolution modules: short-low (SL: 5.2–14.5 μm, 3.6 arcsec × 57 arcsec slit) and long-low (LL: 14.0–38.0 μm, 10.5 arcsec × 168 arcsec slit). Each module comprises two submodules: SL1 and SL2 (SL first and second order), and LL1 and LL2 (LL first and second order), which together cover the wavelength range from 5.2 to 38 μm. Off-source observations were taken to perform sky and zodiacal light subtraction. The data were obtained under different program identifications (PIDs) and investigators. This information is summarized in Table 2.

The spectra were obtained from the *Spitzer* heritage archive provided by the *Spitzer* Science Centre (SSC). Note that no IRS data are available for 3C 277.3 and 4C 73.08. For all observed sources apart from 3C 405, the BCD sets were downloaded and reduced as described by Dicken et al. (2012). For 3C 405, the post-BCD set was downloaded (a source not considered in Dicken et al. 2012), and we median-combined the nodded spectra and scaled the fluxes of data obtained with modules SL1, SL2 and LL2 to that of the LL1 module, using interactive data language (IDL) routines written expressly for the purpose. A scaling of the fluxes between SL and LL is needed, in some cases, owing to the flux difference caused by the objects being partially extended, pointing errors, or poor calibration owing to peak-up saturation of the detector.

3 ANALYSIS OF THE POINT-SOURCE IDENTIFICATION AT NEAR- AND MID-IR WAVELENGTHS

3.1 Detection of AGNs at near-IR wavelengths: *HST*

The identification of unresolved point sources can be difficult, and therefore we apply and compare different approaches in order to investigate the true rate of occurrence of nuclear point sources in radio galaxies. We determine the presence or not of unresolved sources when the galaxy meets three out of four of the following criteria.

(i) **By eye.** Test whether, after performing an eye inspection of the central images, an Airy ring is clearly visible in the image.

(ii) **Azimuthally averaged profile.** Test whether an Airy ring is detected in the azimuthally averaged radial intensity profile.

(iii) **FWHM.** Test whether the full width at half-maximum (FWHM) of the central core of the radial intensity profile is comparable to the resolution achieved by the *HST*.

(iv) **Unsharp masking.** Test whether, when subtracting the smoothed image from the original, traces of a point spread function (PSF) – including the first Airy ring – are detected.

For approach (ii), we plotted the intensity profiles with RADPROF in IRAF using a maximum radial aperture size of 20 pixels, and a one-pixel-step bin. This approach removes some of the ambiguities involved in the 'by eye' method. In particular, an Airy ring is more clearly visible in the intensity profile than in a straightforward visual inspection of the images.

To estimate the FWHM of the core source in approach (iii), we fitted the intensity profile of method (ii) with a cube spline of order five using RADPROF. Then, the fitted FWHM of the radial profile was measured. To take into account the background galaxy, we set the background as the intensity in an annulus of diameter slightly larger than the position of the first Airy ring and with width $\Delta = 0.2$ arcsec. Approach (iii) is clearly more quantitative and removes some of the ambiguities involved in the 'by eye' method. However, there are some weaknesses in this approach: (1) the fitted profile is affected by the Airy ring; and (2) the fitting is potentially affected by the radial profile of the underlying starlight distribution, especially if the starlight distribution rises steeply towards the nucleus. These difficulties will affect the FWHM, resulting in an uncertain AGN detection rate.

For approach number (iv), the smoothed images were created using the SMOOTH function in IDL with a boxcar of 6 × 6 pixels. We subtracted the smoothed *HST* image from the original (non-smoothed) image to examine traces of a PSF in their residual.

Table 3 shows the unresolved core source detection results obtained by applying all four methods to the images. We consider method (iv), unsharp masking, to be the most reliable as it allows the most certain detection of an unresolved core source. However, based on Table 3, in general the four techniques show a high level of agreement. Fig. 1 shows *HST* images at 2.05 μm after applying the unsharp masking method. It is notable that, in the case of 3C 305 and 3C 433, the point sources are so strong that other features of the PSF are clearly visible. Adopting the criterion that the unresolved nucleus is detected when the source meets three out of four of the approaches described above, we find the percentages of unresolved nucleus detection at the four near-IR wavelengths. The sources where the near-IR point source was detected are presented in Table 4. We find that 8 out of 10 (80 per cent) of the radio galaxies of our complete *HST* sample show an unresolved nucleus at 2.05 μm (3C 33, 3C 98, 3C 236, 3C 277.3, 3C 285, 3C 433, 3C 452 and 4C 73.08), and 10 out of 13 (77 per cent) of the extended sample (point sources also detected in 3C 293 and 3C 305); at 1.7 μm we have detected an unresolved core source in 7 out of 10 (70 per cent) of the sources in the complete *HST* sample, and in 8 out of 12 (72 per cent) for the sources in the extended *HST* sample; at 1.45 μm an unresolved source is detected in 6 out of 10 (60 per cent) of the sources in the complete *HST* sample (there are no 1.45 μm images for the three extra sources in the extended *HST* sample); and at 1.025 μm an unresolved source is detected in 3 out of 10 (30 per cent) of the sources in the complete *HST* sample, and in 3 out of 12 (25 per cent) of the sources in the extended *HST* sample.

3.1.1 *Comparison with other studies*

The nuclear properties of FRI/FRII radio galaxies were explored using optical *HST* observations by Chiaberge, Capetti & Celotti (2000, 2002). Chiaberge et al. (2002) reported a compact core source (CCS) detection in 32 per cent (6 out of 19) of the NLRGs in their sample at 7000 Å with redshift $z \lesssim 0.1$ (redshifts comparable to those in our sample). As expected, when comparing the results of Chiaberge et al. (2002) with the fraction of point-source detection at 2.05 μm (80 per cent for the complete *HST* sample, and 77 per cent for the extended sample), a higher unresolved core source detection rate is obtained at longer wavelengths than at shorter wavelengths.

Regarding the CCS detection rate at near-IR wavelengths, Baldi et al. (2010) analysed a sample of 3CR galaxies, observed with NIC2 on the *HST* at 1.6 μm. Taking only the FRII-NLRGs with redshifts comparable with those of our sample ($z \lesssim 0.1$), a CCS is reported in 58 per cent (11 out of 19) of the sources. As expected, the CCS detection rate at 1.6 μm is lower than the 80 per cent found at 2.05 μm in the current study (77 per cent for the extended sample), and than the 70 per cent detection rate at 1.7 μm for the

Table 3. Table showing whether an unresolved source is detected or not according to the four criteria applied to the images. An unresolved source detection is marked with a √. The '∼' symbol indicates barely seen. For method (iii), the FWHM is given. A core source detection is considered when the source meets three out of the four criteria.

Source	1.025-μm approach				1.45-μm approach				1.7-μm approach				2.05-μm approach			
	(i) By eye	(ii) Azimuthal	(iii) FWHM (arcsec)	(iv) Unsharp masking	(i) By eye	(ii) Azimuthal	(iii) FWHM (arcsec)	(iv) Unsharp masking	(i) By eye	(ii) Azimuthal	(iii) FWHM (arcsec)	(iv) Unsharp masking	(i) By eye	(ii) Azimuthal	(iii) FWHM (arcsec)	(iv) Unsharp masking
3C 33	√	∼	0.23 ✗	∼	√	∼	0.19 ✗	√	√	√	0.15 √	√	√	√	0.16 √	√
3C 98	∼	∼	0.41 ✗	∼	√	∼	0.34 ✗	∼	√	∼	0.27 ✗	∼	√	∼	0.24 ✗	√
3C 192	✗	∼	0.27 ✗	✗	✗	∼	0.32 ✗	✗	∼	∼	0.34 ✗	✗	✗	✗	0.33 ✗	✗
3C 236	∼	∼	0.23 ✗	√	✗	∼	0.17 ∼	√	∼	√	0.15 √	√	√	✗	0.18 √	√
3C 277.3	∼	✗	0.30 ✗	✗	✗	✗	0.27 ✗	✗	∼	∼	0.19 ∼	∼	√	∼	0.22 ∼	√
3C 285	✗	✗	0.14 ✗	✗	✗	✗	0.18 ✗	✗	✗	✗	0.21 ✗	✗	√	∼	0.17 √	√
3C 321	✗	✗	0.26 ✗	✗	✗	✗	0.21 ✗	✗	✗	✗	0.26 ✗	✗	✗	✗	0.26 ✗	✗
3C 433	√	∼	0.09 √	∼	√	√	0.08 √	√	√	√	0.07 √	√	√	√	0.13 √	√
3C 452	√	✗	0.25 ✗	✗	√	∼	0.21 ✗	√	√	∼	0.14 √	∼	√	√	0.18 √	√
4C 73.08	∼	∼	0.23 ✗	∼	∼	∼	0.26 ✗	√	√	∼	0.23 ✗	∼	√	∼	0.22 ∼	√
3C 293	✗	✗	0.25 ✗	✗	No data	No data	No data	No data	No data	No data	No data	No data	√	✗	0.21 √	√
3C 305	No data	No data	No data	No data	No data	No data	No data	No data	∼	∼	0.11 √	√	√	√	0.19 √	√
3C 405	✗	✗	0.09 √	✗	Out field	Out field	Out field	Out field	Out field	Out field	Out field	Out field	✗	✗	0.16 √	✗

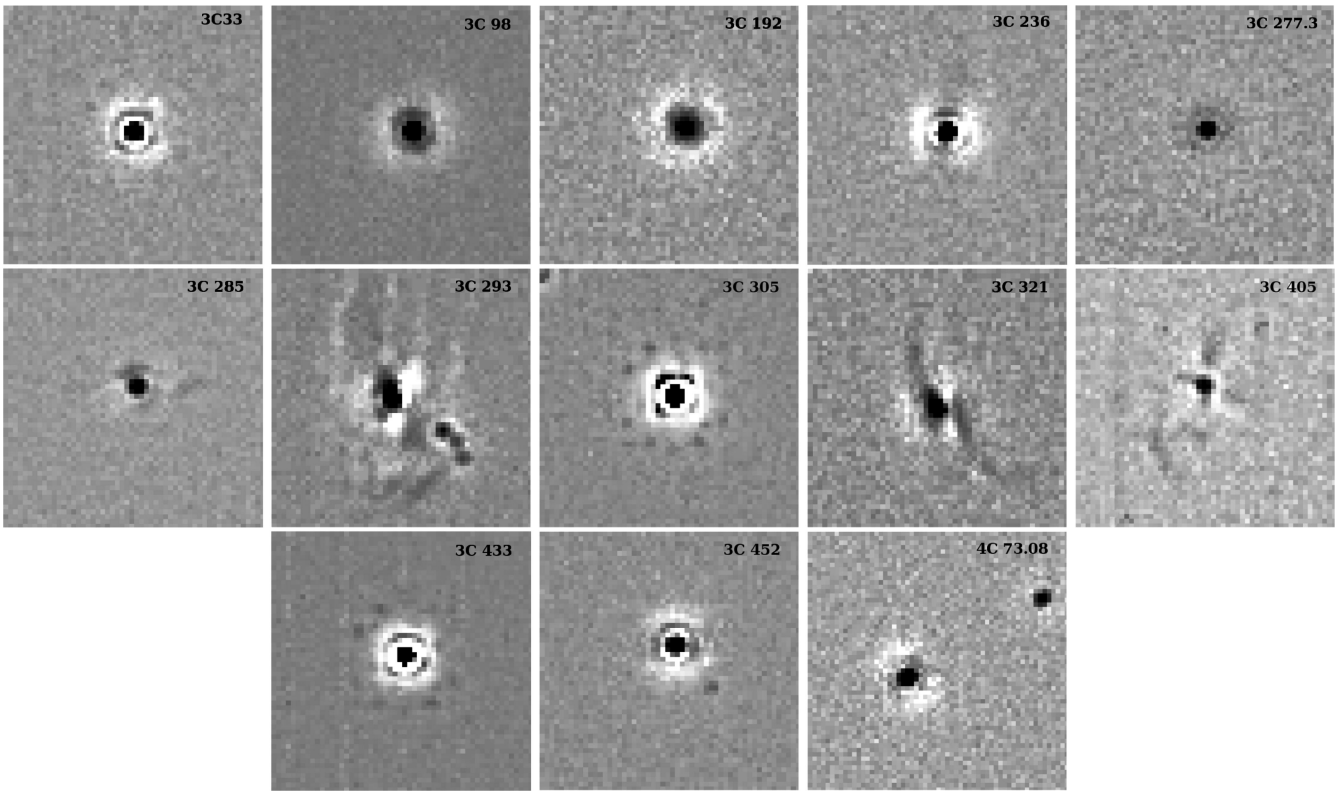

Figure 1. *HST* images at 2.05 μm after applying the unsharp masking method. 4 arcsec × 4 arcsec fields. The images are shown in linear grey-scale.

sources in our complete *HST* sample (72 per cent for the extended sample). However, the 1.6-μm CCS detection rate (58 per cent) is slightly lower than the point-source detection rate at 1.45 μm (60 per cent for both the complete sample and the extended sample), but, given the small size of our *HST* samples, these differences are not statistically significant. Furthermore, Baldi et al. (2010) use NIC2, which has worse sampling than our 1.45-μm NIC1 images.

Marchesini, Capetti & Celotti (2005) analysed a subsample of 3CR radio galaxies using ground-based observations with the Telescopio Nazionale Galileo (TNG) at 2.15 μm (K' band). They detected a central point source in 60 per cent (4 out of 7) of the NLRGs with $z \lesssim 0.1$, based on the $R - K'$ ([0.7μm]−[2.15 μm]) colour profile. The 60 per cent detection rate is lower than the point-source detection rate at 2.05 μm of 80 per cent for our complete sample (or 77 per cent for the extended sample). However, the 2.15-μm ground-based observations are affected by poor resolution owing to seeing effects, which could lead to low nuclear detection rates.

The point source detection rates at the analysed wavelengths are presented in Fig. 2. The potential of longer near-IR wavelengths to

Table 4. Sources where the near-IR unresolved core source was detected (marked with a √) or undetected (marked with a ✗). The '∼' symbol indicates barely seen (and upper limits to its flux are estimated: we also determined upper limits for all sources in which the point source is not detected at 2.05 μm). At the bottom of the table the percentages are presented for the sample (and for the extended sample in parentheses).

Source	1.025 μm	1.45 μm	1.7 μm	2.05 μm
3C 33	√	√	√	√
3C 98	∼	√	√	√
3C 192	✗	✗	✗	✗
3C 236	√	√	√	√
3C 277.3	✗	✗	√	√
3C 285	✗	✗	✗	√
3C 321	✗	✗	✗	✗
3C 433	√	√	√	√
3C 452	✗	√	√	√
4C 73.08	∼	√	√	√
3C 293	✗	No data	No data	√
3C 305	No data	No data	√	√
3C 405	✗	Out field	Out field	✗
	30 per cent (25 per cent)	60 per cent (60 per cent)	70 per cent (72 per cent)	80 per cent (77 per cent)

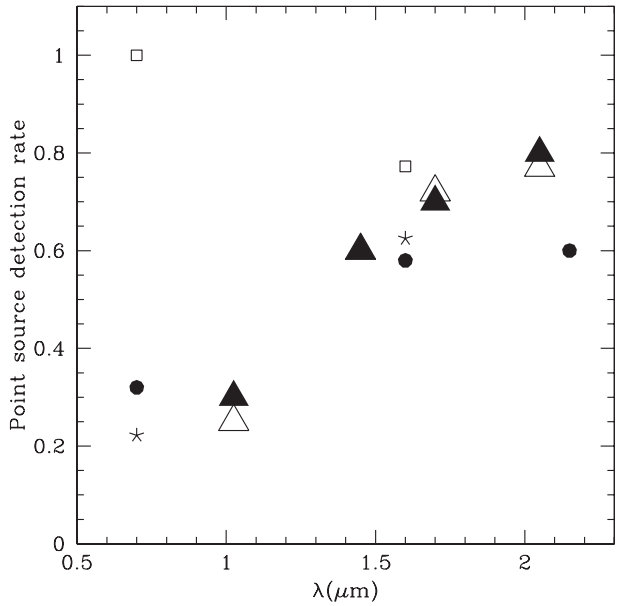

Figure 2. Unresolved core source detection rates for our complete *HST* sample (solid triangles), and for the extended sample (open triangles). Solid circles represent the NLRGs at similar redshifts to our sample ($z \lesssim 0.1$) measured at 7000 Å by Chiaberge et al. (2000), at 1.6 μm by Baldi et al. (2010), and at 2.15 μm by Marchesini et al. (2005). FRII-WLRGs (asterisks) and FRIs (squares) at redshift $z \lesssim 0.1$ are also plotted for comparison. Note how the unresolved core detection rate increases towards longer wavelengths for both NLRGs and FRII-WLRGs.

directly detect obscured AGNs has been demonstrated. The point-source detection rate increases towards longer near-IR wavelengths. Fig. 2 also shows the detection rate, differentiating between FRII weak-line radio galaxies (FRII-WLRGs) and FRIs (asterisks and squares, respectively; Chiaberge et al. 2000, 2002; Baldi et al. 2010). We made this differentiation for the following reason. In the context of the orientation-based unified scheme, FRIs and FRII-WLRGs are thought to have similar intrinsic AGN properties – perhaps lacking a torus and classical accretion disc (Hardcastle, Evans & Croston 2009; Buttiglione et al. 2010). Moreover, there is no convincing evidence for the presence of a dusty torus in most WLRGs (van der Wolk et al. 2010; Leipski et al. 2009). However, we found that at optical wavelengths (7000 Å), 100 per cent (16 out of 16) of the FRIs with redshifts $z \lesssim 0.1$ show an unresolved core source (Chiaberge et al. 2002), and that 22 per cent (2 out of 9) of the FRII–WLRGs with redshifts $z \lesssim 0.1$ show an unresolved core source (Chiaberge et al. 2002). Therefore it is surprising to find such differences in the optical CCS detection rate. On the other hand, the FRII-WLRGs from Chiaberge et al. (2002, asterisk) have a similar optical CCS detection rate to our FRII-NLRGs at similar redshifts. At longer near-IR wavelengths (1.6 μm), the percentages are not so different: 62 per cent (5 out of 8) of the FRII-WLRGs with redshift $z \lesssim 0.1$ show an unresolved core source (Baldi et al. 2010), and 77 per cent (17 out of 22) of the FRI radio galaxies with redshift $z \lesssim 0.1$ show an unresolved core source (Baldi et al. 2010).

3.1.2 AGN flux estimation

It is important to estimate the flux of an AGN, free of the contribution from starlight, in order to determinate the degree of extinction suffered by the AGN. Powerful radio AGNs are almost invariably hosted by elliptical galaxies (Zirbel 1996; Ramos Almeida et al. 2012). The bright compact nucleus of 3C 433 dominates the near-IR light, making the underlying host galaxy difficult to detect (Madrid et al. 2006; Ramírez et al. 2009). However, the other sources in our *HST* sample have fainter point sources compared with 3C 433; this makes the determination of point-source fluxes more challenging. Hence, it is necessary to correct for the starlight from the underlying host galaxies in order to obtain the AGN fluxes free of starlight contamination.

To tackle this problem, we estimated the unresolved core flux by modelling the images with a combination of a nuclear point source represented by a TinyTim-generated PSF (Krist & Hook 2004) and a Sérsic profile to take into account the light of the underlying host galaxy. This method was executed using GALFIT (Peng et al. 2002).

The Sérsic profile has the following functional form:

$$I = I_0 \exp\left[-\kappa\left(\frac{r}{r_0}\right)^{1/n}\right], \quad (1)$$

where $1/n$ is the concentration parameter (n is known as the Sérsic index), κ is a dependent variable of n, and I_0 is the surface intensity at the effective radius r_0. For $n = 1$, the profile is exponential, characteristic of the discs of spiral galaxies, while $n = 4$ corresponds to a de Vaucouleurs profile, characteristic of elliptical galaxies. This method to estimate the fluxes assumes that the AGN luminosity profile has the shape of a PSF. Neighbouring sources were masked out during the fitting. To avoid possible degeneracies in the applied fitting technique, we ran GALFIT, varying the initial values to check the convergence of our results. In addition, we compared our PSF fluxes with a trial-and-error PSF subtraction (i.e. not relying on a particular model for the underlying galaxy), and found consistent results. The near-IR AGN fluxes are tabulated in Table 5, together with the calculated spectral indices of the near-IR SEDs. Although we did not detect an unresolved core source in 3C 192, 3C 321 and 3C 405, in these cases we estimated an upper limit to the 2.05-μm fluxes applying the same procedure as explained above (fitting a PSF plus a Sérsic profile with GALFIT), and then fixed the free parameters of the Sérsic profile to subtract a PSF only using a trial-and-error approach until an unphysical hole appeared owing to over-subtraction.

Table 5. *HST* core fluxes ($\times 10^{-5}$ Jy) at the central wavelength of the filters estimated using PSF+Sérsic. 'No PS' indicates undetected point source. '<' is the upper limit for undetected PS flux. $\alpha_{\rm NIR}$ is the near-IR SED spectral index ($F_\nu \propto \nu^{-\alpha_{\rm NIR}}$).

Source	F110W 1.025 μm	F145M 1.45 μm	F170M 1.7 μm	POL-L 2.05 μm	$\alpha_{\rm NIR}$
3C 33	0.49 ± 0.10	1.8 ± 0.2	2.0 ± 0.4	23.0 ± 1.0	5.0 ± 1.6
3C 98	<0.041	0.19 ± 0.52	0.93 ± 0.26	5.5 ± 0.3	9.7 ± 1.3
3C 192	No PS	No PS	No PS	<1.9	–
3C 236	1.4 ± 0.1	1.8 ± 0.3	5.3 ± 0.5	16.0 ± 1.0	3.5 ± 1.1
3C 277.3	No PS	No PS	0.55 ± 0.38	2.9 ± 0.3	–
3C 285	No PS	No PS	No PS	9.6 ± 0.3	–
3C 321	No PS	No PS	No PS	<3.6	–
3C 433	1.9 ± 0.7	16.0 ± 3.0	46.0 ± 4.0	140.0 ± 10.0	6.2 ± 0.1
3C 452	No PS	0.40 ± 0.19	2.4 ± 0.5	22.0 ± 1.0	11.6 ± 0.2
4C 73.08	<0.57	0.75 ± 0.27	1.2 ± 0.5	5.4 ± 0.3	5.8 ± 1.5
3C 293	No PS	No data	No data	10.0 ± 3.0	–
3C 305	No data	No data	21.0 ± 2.0	28.0 ± 3.0	–
3C 405	No PS	Out field	Out field	<6.2	–

3.2 AGN at mid-IR wavelengths: IRAC

The lower extinction experienced at longer IR wavelengths may allow us to have a clearer view of the inner regions of AGNs. The sensitivity of *Spitzer* is orders of magnitude greater than that of previous satellites working at mid- to far-IR wavelengths (e.g. *Infrared Astronomical Satellite*, *IRAS*; *Infrared Space Observatory*, *ISO*). Hence, with IRAC we can potentially achieve the direct detection of a hidden AGN in a NLRG.

However, the fact that the *Spitzer* has much lower resolution than the *HST* means that the measured AGN fluxes based on aperture photometry could be highly contaminated by starlight. To enclose most of the point-source light and avoid background contamination, aperture photometry was performed within a 6-arcsec-diameter aperture using the STARLINK GAIA package. The starlight contribution was subtracted from the photometry in the following way.

First, we measured the 2.05-μm flux of the starlight from the NICMOS/*HST* images through the same size aperture (6 arcsec diameter), using the residual 2.05-μm image after point-source subtraction (see Section 3.1.2). The 2.05-μm fluxes are closer in wavelength to the mid-IR, more likely to be in the Rayleigh–Jeans tail of the starlight SED, and require less of an extrapolation than the shorter near-IR wavelengths. Therefore, the 2.05-μm images are best suited to estimating the starlight contribution from the host galaxies and to extrapolating to mid-IR wavelengths.

Secondly, we took the 2.15-, 3.6-, 4.5-, 5.8- and 8.0-μm fluxes of normal elliptical galaxies from Temi, Brighenti & Mathews (2008), assuming that they are dominated by starlight. Temi et al. (2008) performed surface photometry of a sample of 18 elliptical galaxies with *Spitzer* at 3.6, 4.5, 5.8, 8.0 and 24 μm, of which 16 have 2MASS (Two Micron All Sky Survey) data at 1.2, 1.6 and 2.15 μm. We fitted a power law to the mid-IR SEDs of the 16 individual normal elliptical galaxies with data from 2.15 to 8.0 μm, and calculated the median spectral index of elliptical galaxies, $\alpha_{\rm EG} = 1.76 \pm 0.03$ ($F_\nu \propto \nu^{-\alpha_{\rm EG}}$). This spectral index ($\alpha_{\rm EG} = 1.76$) is close to the spectral index of the Rayleigh–Jeans tail of a blackbody ($\alpha_{\rm RJ} = 2$), giving confidence that the fluxes from the elliptical galaxies from Temi et al. (2008) are pure starlight, free from the emission of unusual AGNs, starbursts and cool gas.

Thirdly, we used this median spectral index ($\alpha_{\rm EG}$) to extrapolate our measured 2.05-μm starlight flux to the IRAC mid-IR wavelengths, in order to estimate the starlight contamination in our IRAC photometry. We subtracted these estimated starlight fluxes from the measured IRAC photometry fluxes within the 6-arcsec-diameter aperture, to obtain the mid-IR core fluxes free of starlight contribution.

Finally, we applied an aperture correction from an empirically determined curve of flux versus aperture radius, derived from an artificial PSF generated by STINYTIM (Krist 2004), to the 6-arcsec-diameter aperture photometry. The aperture correction factors (total flux / flux within 6 arcsec) are 1.190, 1.198, 1.314 and 1.532 for the 3.6-, 4.5-, 5.8- and 8.0-μm wavelengths, respectively. The final mid-IR AGN fluxes free of starlight, and aperture-corrected, are tabulated in Table 6, together with the calculated spectral indices of the mid-IR SED.

The uncertainty in the AGN flux comes from the uncertainty in the aperture photometry performed on the IRAC–*Spitzer* images (of the order of 1.9 per cent for wavelengths of 3.6 and 4.5 μm, and of 2.1 per cent for wavelengths of 5.8 and 8.0 μm), from the measured starlight flux at 2.05 μm (of the order of 3 to 10 per cent), and from the estimated spectral index for normal elliptical galaxies (of the order of 5.7, 8.5, 10.3 and 13.9 per cent at wavelengths of 3.6, 4.5, 5.8 and 8.0 μm, respectively). The total uncertainties in the IRAC AGN fluxes, taking all these factors into account, are typically 22, 13, 7 and 3 per cent at wavelengths of 3.6, 4.5, 5.8 and 8.0 μm, respectively. Note that the error is smallest for the longer IRAC wavelengths. This is because the extrapolated starlight contribution declines towards longer wavelengths, so while the uncertainty in the extrapolation of the starlight component is large at 8.0 μm, its flux is low compared with the relatively high 8.0-μm IRAC photometry. This is not the case for the 3.6-μm flux. Therefore, the overall uncertainties of the IRAC AGN fluxes are smaller at 8.0 than at 3.6 μm. However, the uncertainties vary substantially from source to source (see Table 6).

We used WISE (Wright et al. 2010) data for 3C 277.3 and 3C 433 (there are no IRAC data for these two sources) at 3.4, 4.6, 12 and 22 μm (bands W1, 2, 3 and 4, respectively), achieving an angular resolution of 6.1, 6.4, 6.5 and 12.0 arcsec in the four bands. WISE performs aperture photometry on the sources and background estimation within an annulus. The adopted aperture size is 8.25 arcsec for W1, 2 and 3, and 16.50 arcsec for W4 (the standard WISE apertures). The annulus has an inner radius of 50 arcsec and a width of 20 arcsec (for all four bands). The fluxes were estimated from the WISE-band magnitudes using zero-magnitude flux densities based on observations of Vega.[2] As with IRAC photometry, we subtracted the extrapolated starlight from the WISE fluxes. Aperture correction was then applied, and the total flux of the source estimated. The aperture correction factors are 1.32, 1.39, 2.08 and 1.76 for the 3.4-, 4.6-, 12- and 22-μm wavelengths, respectively, for the used apertures.

3.2.1 *AGN detection rate at mid-IR wavelengths*

The near- to mid-IR SEDs (*HST*–*Spitzer*-based SEDs) of the radio galaxies are presented in Fig. 3, in which the approach used to estimate the starlight contamination to the IRAC photometry is illustrated graphically. The starlight residual after PSF subtraction at 2.05 μm, and the starlight flux extrapolated to the IRAC wavelengths are indicated by stars. It is clear from Fig. 3 that the mid-IR SED turns up towards shorter mid-IR wavelengths for 3C 192, and

[2] For further details see http://wise2.ipac.caltech.edu/docs/release/allsky/expsup/sec4_4h.html.

Table 6. IRAC AGN fluxes ($\times 10^{-3}$ Jy). '<' indicates upper limits for undetected AGNs. $\alpha_{\rm MIR}$ is the mid-IR SED spectral index ($F_\nu \propto \nu^{-\alpha_{\rm MIR}}$).

Source	3.6 μm	4.5 μm	5.8 μm	8.0 μm	$\alpha_{\rm MIR}$
3C 33	$<1.9 \pm 0.4$	4.3 ± 0.3	7.4 ± 0.2	14.8 ± 0.3	2.5 ± 0.2
3C 98	$<2.3 \pm 0.9$	$<2.9 \pm 0.7$	5.4 ± 0.8	10.0 ± 0.3	$>1.9 \pm 0.2$
3C 192	$<0.8 \pm 0.2$	$<0.5 \pm 0.2$	$<0.5 \pm 0.1$	0.8 ± 0.1	–
3C 236	$<1.8 \pm 0.2$	2.6 ± 0.2	3.4 ± 0.1	6.4 ± 0.1	1.6 ± 0.1
3C 277.3	–	–	–	–	– [a]
3C 285	2.3 ± 0.2	3.8 ± 0.2	6.8 ± 0.2	15.7 ± 0.2	2.4 ± 0.6
3C 321	$<1.3 \pm 0.3$	3.6 ± 0.2	9.9 ± 0.2	29.4 ± 0.4	3.9 ± 0.2
3C 433	–	–	–	–	– [a]
3C 452	2.5 ± 0.2	3.9 ± 0.2	6.9 ± 0.2	13.1 ± 0.2	2.1 ± 0.4
4C 73.08	$<1.6 \pm 0.6$	2.3 ± 0.4	4.4 ± 0.2	9.6 ± 0.2	2.3 ± 0.13
3C 293	3.6 ± 0.5	4.6 ± 0.3	7.5 ± 0.3	14.5 ± 0.3	1.8 ± 0.14
3C 305	$<2.4 \pm 0.7$	$<2.1 \pm 0.5$	4.1 ± 0.4	9.5 ± 0.3	$>1.9 \pm 0.5$
3C 405	–	8.0 ± 0.2	–	55.3 ± 0.7	3.4 [b]
WISE	3.4 μm	4.6 μm	12 μm	22 μm	$\alpha_{\rm MIR}$
3C 277.3	0.86 ± 0.03	1.3 ± 0.03	5.8 ± 0.1	11.2 ± 0.9	1.4 ± 0.1
3C 433	28.0 ± 0.1	49.7 ± 0.2	207.9 ± 0.7	448.6 ± 3.8	1.5 ± 0.1

[a]There are no IRAC data (fluxes derived from WISE data; see bottom of the table and main text for details). [b]The uncertainty is impossible to estimate because there are IRAC data only at two wavelengths.

to a smaller extent for 3C 98 and 3C 305. This is an indication of a dominant contribution of starlight from the host galaxy at shorter wavelengths in these sources. On the other hand, the mid-IR photometric points of 3C 285 fall far above the extrapolated starlight, indicative of little starlight contamination.

Taking a 3σ difference between the extrapolated starlight and measured *Spitzer* fluxes as the criterion to decide whether the AGN is detected above the starlight contribution, we found that, at 8.0 μm, the AGN component is detected in all the sources, both in our complete *HST* sample and in the extended sample. The sources for which the mid-IR point source was detected are presented in Table 7. The low detection rate at the shorter wavelengths is a result of the difficulty of detecting the AGN above the stellar component because of the low spatial resolution and large apertures. In Fig. 4 the mid-IR detection rates are plotted, together with the optical and near-IR point-source detection rates. These highlight that the fraction of direct AGN detection at 8 μm is higher than that deduced at 2.05-μm wavelengths using NICMOS–*HST* data.

In the cases of 3C 277.3 and 3C 433 – for which there are no IRAC data and for which we used data from WISE – the starlight contribution from the host galaxy is negligible for 3C 433 at all WISE wavelengths (see Fig. 3), but is significant for 3C 277.3 at 3.4 and 4.6 μm (the two shortest wavelengths of WISE). Given that the WISE photometric fluxes for 3C 433 are so much higher than the starlight contamination, we can say with certainty that its AGN would be detected at all IRAC wavelengths; therefore we include this object in the 8.0-μm AGN detection statistics. This is not the case for 3C 277.3, because its SED shows a substantial starlight contribution at 3.4 and 4.6 μm, suggesting that its AGN would not be clearly detected at 3.6 and 4.5 μm with IRAC, and making it uncertain that the AGN would be detected at 5.8 and 8.0μm in this object.

4 ANALYSIS: ESTIMATING THE EXTINCTION THROUGH THE TORUS

Given that the unresolved point-source detections in the sources possibly indicate a direct view of the obscured AGN, the extinction caused by the torus – quantified as A_V (the extinction in the optical V band) – may be estimated under the assumption that the inner regions of the AGN are being extinguished by a screen of dust (Antonucci 1993; Urry & Padovani 1995), in this case a foreground torus structure. In this section we present the optical extinction estimates derived from the near-IR SED spectral index, from the X-ray luminosity, from the column density derived from X-ray data, from the mid-IR SED spectral index, and based on the mid-IR silicate absorption feature.

4.1 Near-IR SED

In the cases where the near-IR point source was detected at more than one near-IR wavelength, the point-source fluxes were estimated, and their near-IR SED spectral index $\alpha_{\rm NIR}$ calculated ($F_\nu \propto \nu^{-\alpha_{\rm NIR}}$). There were cases for which, at the shorter wavelengths, the dust obscuration made it difficult to detect a point source. For this reason, in some cases the near-IR SED was fitted without considering the 1.025-μm core flux. The spectral indices of each source are presented in column 6 of Table 5.

By comparing this 'reddened' power-law index with the mean unreddened power-law index of radio-loud quasars, $\overline{\alpha}_{\rm QSO} = 0.97\pm^{0.65}_{1.64}$ (Simpson & Rawlings 2000), it is possible to estimate the 2.05-μm extinction by de-reddening the SED until the slope agrees with the mean quasar slope. We used a typical Galactic extinction law $A_\lambda \propto \lambda^{-\gamma}$ for the near-IR range ($\gamma = 1.7$; Mathis 1990) to de-redden the radio galaxy SEDs. The equivalent optical extinction is then straightforward to calculate ($A_V/A_{2.05\mu{\rm m}} = [0.55/2.05]^{-1.7} = 9.36$; Mathis 1990). The extinctions estimated by this method, A_V(NIR), are tabulated in column 2 of Table 8.

4.2 X-ray luminosity

The extinction can also be estimated by using the unabsorbed monochromatic X-ray luminosity at 2 keV of the obscured nuclear sources (Evans et al. 2006; Hardcastle, Evans & Croston 2006; Hardcastle et al. 2009), where available (see column 3 of

Table 8). First, using the X-ray-to-1.0 μm luminosity relation in Kriss (1988), and accounting for the different cosmological parameters used in that paper, we estimated the intrinsic flux at 1.0 μm using the luminosity distance from the NASA/IPAC extragalactic data base (NED). By comparing this with our measured flux at 1.025 μm, the near-IR extinction can be derived. Finally, the equivalent optical extinction was derived using the Galactic extinction law of Mathis (1990 : $A_V/A_\lambda = [0.55/\lambda]^{-1.7}$). In cases for which the 1.025-μm point source is not detected, or is uncertain because of the effect of dust extinction, more steps were required to obtain to the optical extinction: after deriving the luminosity at 1.0 μm, the $L_{2.05\,\mu m}$ versus $L_{1.0\,\mu m}$ relationship (Kriss 1988, his fig. 2) was used to find $F_{2.05\,\mu m}$, using the corresponding luminosity distance. By comparing this flux with our measured 2.05-μm flux we derived the extinction $A_{2.05\,\mu m}$. Again, the equivalent optical extinction was obtained using the law of Mathis (1990). The optical extinctions derived by this method, $A_V(L_{X-ray})$, are tabulated in column 4 of Table 8.

It is interesting that 3C 305 gives a negative optical extinction based on the X-ray luminosity [$A_V(L_{X-ray}) = -21.3 \pm 9.0$ mag], consistent with the unabsorbed power law fitted to its X-ray spectrum (see next subsection). This strongly suggests that the X-ray luminosity has been underestimated: perhaps the source is Compton-thick and we are only seeing scattered light in X-rays, or it is in a 'switched off' phase in the evolution of its variable X-ray AGN. In fact, 3C 305 has a mid-IR spectrum that shows very strong high

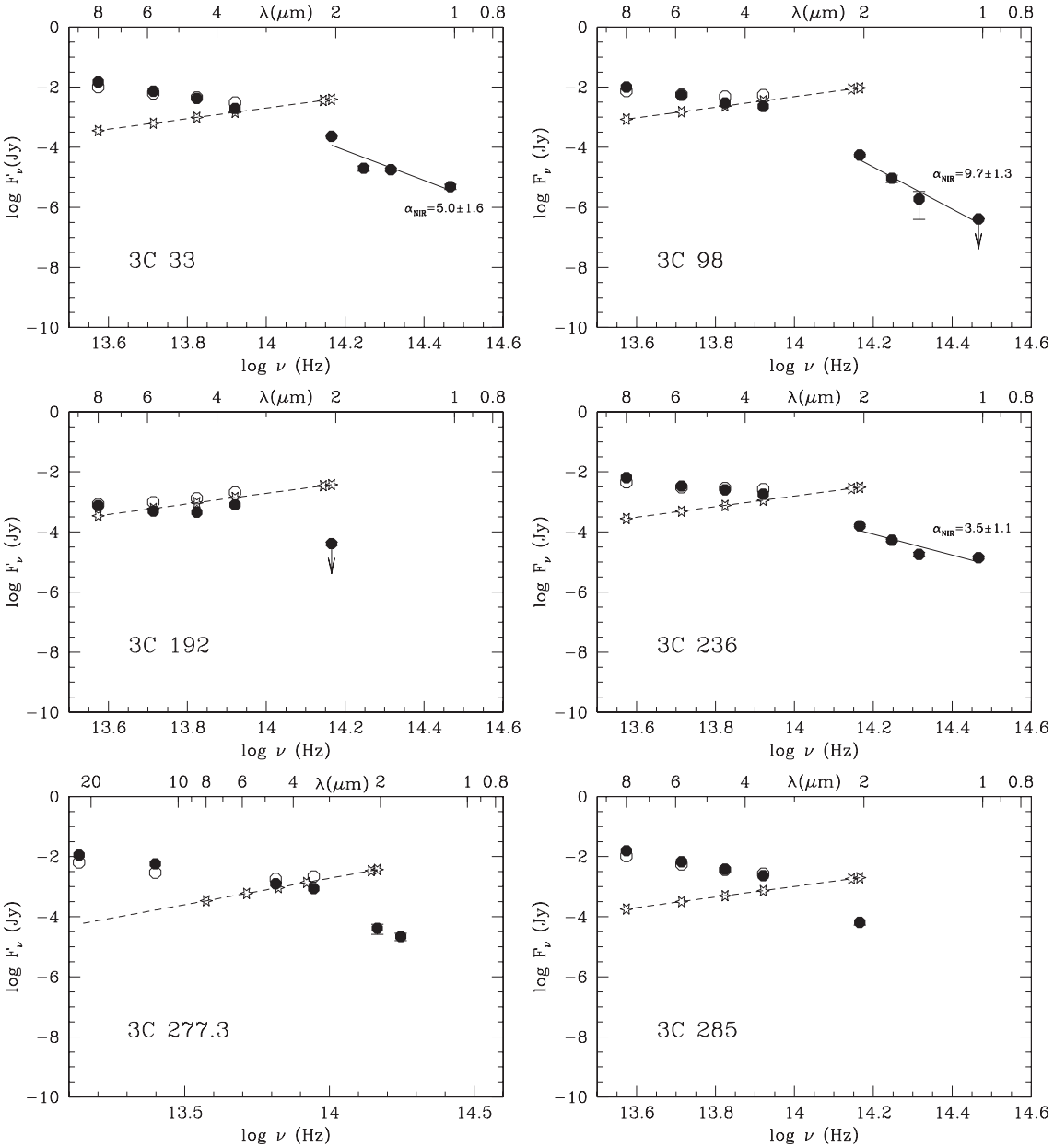

Figure 3. Near- to mid-IR AGN SEDs. Solid dots represent the near- and mid-IR AGN fluxes (*HST* and *Spitzer* respectively) that have been starlight-subtracted and aperture-corrected. The solid line is the power-law fit of the *HST* fluxes. The open circles show the measured fluxes before starlight and aperture correction. The dashed line represents the extrapolation of the *HST*-derived 2.05 μm starlight flux to longer wavelengths, and the star symbols represent the starlight fluxes. For 3C 277.3 and 3C 433 the mid-IR data are taken from WISE (there are no IRAC data for these sources).

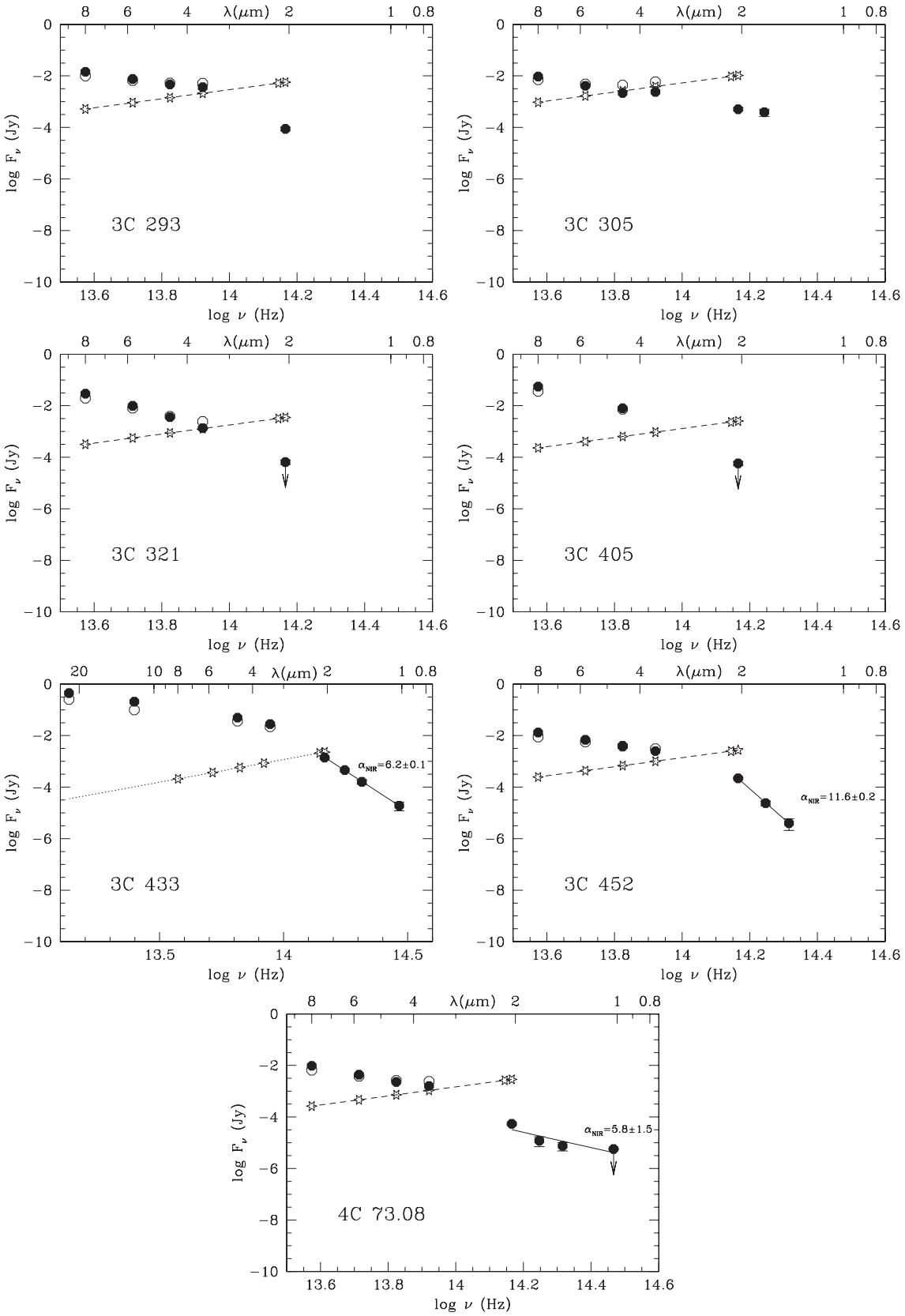

Figure 3 – *continued*

Table 7. Sources for which the mid-IR AGN core source were detected (marked with a √), or undetected (marked with a ✗). At the bottom of the table the percentage detection rates are presented for the sample (and for the extended sample in parentheses).

Source	3.6 μm	4.5 μm	5.8 μm	8.0 μm
3C 33	✗	√	√	√
3C 98	✗	✗	√	√
3C 192	✗	✗	✗	√
3C 236	✗	√	√	√
3C 277.3	No data	No data	No data	No data
3C 285	√	√	√	√
3C 321	✗	√	√	√
3C 433	No data	No data	No data	√
3C 452	√	√	√	√
4C 73.08	✗	√	√	√
3C 293	√	√	√	√
3C 305	✗	✗	√	√
3C 405	No data	√	No data	√
	25 per cent (30 per cent)	75 per cent (73 per cent)	88 per cent (90 per cent)	100 per cent (100 per cent)

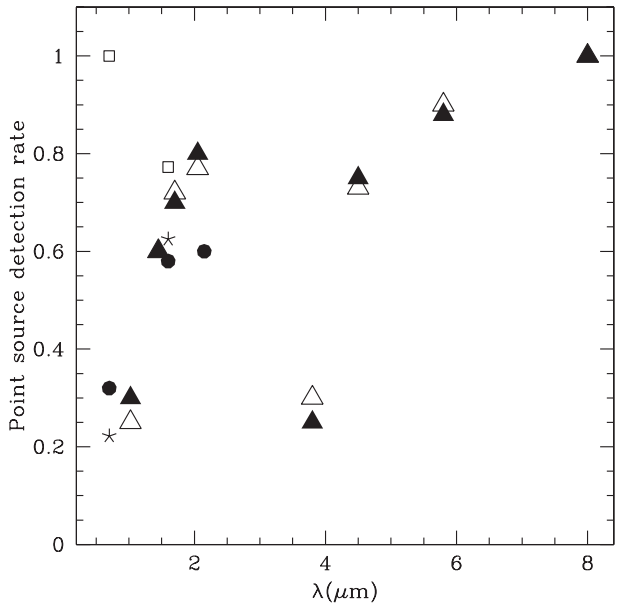

Figure 4. Unresolved core source detection rates, as in Fig. 2, but including the IRAC mid-IR detection rates for our complete *HST* sample (solid triangles), and for the extended sample (open triangles). Note that the unresolved core source detection rate improves with wavelength for the FRII sources from 2.05 to 8.0 μm; the lower rates of detection at 3.6, 4.5 and 5.8 μm are probably the result of the difficulties in detecting AGNs above the starlight with the large *Spitzer* aperture.

ionization emission lines ([O IV]), suggesting that it hosts a luminous AGN (Dicken et al. 2012).

4.3 X-ray column density

The third method to estimate the extinction involves using the standard Galactic dust-to-gas ratio $(A_V/\mathrm{N_H})^{\mathrm{G}} = 5.3 \times 10^{-22}$ mag cm^2 (Bohlin, Savage & Drake 1978), and the atomic hydrogen column density, N_{H}, derived from X-ray observations. The N_{H} and optical extinctions are shown in columns 5 and 6 of Table 8, respectively. For 3C 305, the X-ray spectrum has been fitted using an unabsorbed power law (Hardcastle et al. 2009). The optical extinctions based on the X-ray column density using the standard dust-to-gas ratio (Bohlin et al. 1978) are considerably higher than the optical extinctions estimated from the near-IR SED and X-ray luminosity: 2 to 8 times higher in most cases (even up to 15 and 26 times for 3C 321 and 4C 73.08, respectively).

Several studies suggest that AGNs have a lower dust-to-gas ratio than the Galactic value (Maccacaro, Perola & Elvis 1982; Reichert et al. 1985; Maiolino et al. 2001). Maiolino et al. (2001) analysed a sample of 19 radio-quiet AGNs of various classes (quasars, Seyferts 1, 2 and intermediate types) whose X-ray spectra show evidence for absorption associated with an obscuring torus, and whose optical and/or IR spectra show broad lines that are not completely absorbed by the dust associated with the X-ray absorber, to verify the low dust-to-gas ratio noted in some AGNs. By comparing the reddening towards the BLR with the gaseous N_{H} inferred from the X-rays, Maiolino et al. (2001) found that the dust-to-gas ratio is lower than the Galactic standard value. The interpretation that Maiolino et al. (2001) gave to their results is that the circumnuclear region of the AGN is composed of large grains, because the small grains, responsible for absorbing most of the optical radiation, are depleted, or become large grains by a coagulation process. To ascertain whether our sample of radio-loud AGNs also follows this trend of having a lower dust-to-gas ratio than the Galaxy, we plotted the ratio of the optical extinction, A_V(NIR), estimated from our near-IR SED results (using $E(B-V) = A_V/3.1$; Maiolino et al. 2001), with the column density derived from X-ray observations, on the diagram of Maiolino et al. (2001, his fig. 1; see Fig. 5). It is clear that our sample follows the same trend as found by Maiolino et al. (2001) for radio-quiet AGNs, suggesting that radio-loud AGN sources also have lower dust-to-gas ratios than the standard dust-to-gas ratio of the Galaxy (except for 3C 236).

Therefore, we corrected the dust-to-gas ratio $(A_V/N_{\mathrm{H}})^{\mathrm{G}}$ for AGNs using the results in fig. 1 of Maiolino et al. (2001, our Fig. 5) to obtain the range $A_V/N_{\mathrm{H}} = 3.1 \times 10^{-23} - 1.83 \times 10^{-22}$ mag cm^2 for the upper and lower limits, respectively. Considering fig. 1 of Maiolino et al. (2001, our Fig. 5), the upper limit was estimated taking the mean A_V/N_{H} of the seven upper points, while for the minimum we took the mean of the nine lower points, in both cases utilizing the data extractor DEXTER (Demleitner et al. 2001). The computed extinction, $A_V(N_{\mathrm{H}})$, using the results of Maiolino et al. (2001), is tabulated in column 7 of Table 8.

The extinctions based on the lower dust-to-gas ratios of Maiolino et al. (2001) give results that are more consistent with the optical extinctions estimated from the near-IR SED and from the X-ray luminosity than the standard dust-to-gas ratio of the Galaxy . Therefore, applying the results of Maiolino et al. (2001), the optical extinctions estimated by the three different methods are all in reasonable agreement.

4.4 Mid-IR SED

To estimate the extinction suffered by the AGNs in the mid-IR, we took the mid-IR AGN photometry estimated in Section 3.2, and fitted the mid-IR SEDs with a power law. Following the technique we used to estimate the extinction in the case of the near-IR measurements (see Subsection 4.1), we de-reddened the mid-IR SEDs until the spectral index matched the unabsorbed mid-IR spectral index of a type 1 AGN. We excluded 3C 192 because its IRAC fluxes are severely contaminated by starlight. Because 3C 98 and 3C 305 have starlight contamination at 3.6 μm, we did not use this wavelength to estimate the spectral index for these two sources.

Table 8. Extinction estimates for the core sources in the NLRGs, A_V (mag). Column 1, source name from the 3CRR catalogue (Laing et al. 1983); column 2, extinction based on the near-IR SED (A_V(NIR)); column 3, X-ray unabsorbed luminosity of the core; column 4, extinction based on the X-ray luminosity ($A_V(L_{\rm X\text{-}ray})$); column 5, X-ray density column; column 6, extinction using the standard Galactic ratio ($(A_V/N_{\rm H})^{\rm G} = 5.3 \times 10^{-22}$ mag cm^2, Bohlin et al. 1978); column 7, extinction based on the X-ray column density using the results of Maiolino et al. (2001, $A_V(N_{\rm H})$); column 8, extinction based on the mid-IR SED (A_V(MIR)); column 9, the $\tau_{9.7}$ μm: silicate optical depth; column 10, extinction based on the silicate absorption feature ($A_V(\tau_{9.7})$); column 11, references for the X-ray luminosity and density column used to estimate the optical extinction.

Source	Method									Ref.
	Near-IR SED	X-ray luminosity		X-ray column			Mid-IR SED	Silicate absorption		
	A_V(NIR)	$L_{(2-10){\rm kev}}$	$A_V(L_{\rm X\text{-}ray})$	$N_{\rm H}$ (cm^{-2})	A_V^G	$A_V(N_{\rm H})$	A_V(MIR)	$\tau_{9.7}$	$A_V(\tau_{9.7})$	
3C 33	11.0 ± 5.0	$6.3 \pm 1.3 \times 10^{43}$	25.7 ± 4.0	$3.9 \pm^{0.7}_{0.6} \times 10^{23}$	$206 \pm^{37}_{32}$	12 – 72	86.9 ± 34.4	0.22 ± 0.04	4.1 ± 0.8	a
3C 98	35.6 ± 6.0	$5.4 \pm 1.1 \times 10^{42}$	>27.2	$1.2 \pm^{0.3}_{0.2} \times 10^{23}$	$64 \pm^{16}_{11}$	4 – 22	53.8 ± 33.8	0.00[iii]	0.0	a
3C 192	no PS	$8.5 \pm 1.7 \times 10^{42}$	>47.4	$51.6 \pm^{32.8}_{16.6} \times 10^{22}$	$274 \pm^{175}_{88}$	16 – 95	no PS	0.00[iii]	0.0	b
3C 236	6.0 ± 3.5	$1.5 \pm 0.8 \times 10^{42}$	3.0 ± 4.3	$2.4 \pm^{1.1}_{1.0} \times 10^{22}$	$13 \pm^{6}_{5}$	1 – 4	36.9 ± 32.8	0.30 ± 0.01	5.6 ± 0.35	c
3C 277.3	No SED	$1.4 \pm 0.3 \times 10^{43}$	43.2 ± 11.5	$2.5 \pm^{1.0}_{0.5} \times 10^{23}$	$133 \pm^{53}_{27}$	8 – 46	23.2 ± 14.2	no data	–	d
3C 285	No SED	$2.1 \pm 0.4 \times 10^{43}$	38.2 ± 11.0	$32.1 \pm^{5.5}_{4.6} \times 10^{22}$	$170 \pm^{29}_{24}$	10 – 59	83.4 ± 33.7	1.31 ± 0.25	24.2 ± 4.8	b
3C 321	No PS	$1.2 \pm^{2.0}_{0.6} \times 10^{43}$	>36.1	$1.0 \pm^{0.55}_{0.21} \times 10^{24}$	$551 \pm^{292}_{111}$	32 – 191	171.0 ± 32.7	0.34 ± 0.02	6.3 ± 0.5	e
3C 433	14.6 ± 1.0	$8.3 \pm 1.6 \times 10^{43}$	19.2 ± 4.6	$9.0 \pm 1.0 \times 10^{22}$	48 ± 5.3	3 – 17	28.5 ± 15.0	0.85 ± 0.04	15.7 ± 3.0	f
3C 452	44.0 ± 3.0	$1.0 \pm 0.2 \times 10^{44}$	55.9 ± 12.4	$7.5 \pm^{0.9}_{0.8} \times 10^{23}$	$302 \pm^{48}_{42}$	18 – 105	65.5 ± 33.7	0.15 ± 0.05	2.9 ± 0.5	a
4C 73.08	18.5 ± 8.6	$5.7 \pm^{6.9}_{3.2} \times 10^{42}$	32.4 ± 19.5	$9.2 \pm^{5.4}_{2.9} \pm 10^{23}$	$488 \pm^{286}_{154}$	29 – 169	77.1 ± 33.7	no data	–	g
3C 293	No SED	$7.4 \pm 1.5 \times 10^{42}$	34.9 ± 12.0	$13.1 \pm^{5.1}_{3.5} \times 10^{22}$	$69 \pm^{27}_{20}$	4 – 24	48.6 ± 32.7	1.34 ± 0.25	24.8 ± 4.9	h
3C 305	No SED	$2.6 \pm 0.8 \times 10^{41}$	– [ii]	unabsorbed	–	–	53.8 ± 33.8	0.37 ± 0.01	6.8 ± 0.4	h
3C 405	No PS	3.7×10^{44} [i]	>90.5	$2.0 \pm^{0.1}_{0.2} \times 10^{23}$	$106 \pm^{5}_{11}$	6 – 37	141.4 ± 33.8	0.27 ± 0.02	5.0 ± 0.5	i

Notes: [i] Error not given in the X-ray luminosity by Young et al. (2002). [ii] The optical extinction is negative for 3C 305: -21.3 ± 9.0 (and 3C 236 considering the error bars). It is very likely, based on its emission line properties, that the X-ray luminosity of 3C 305 is substantially underestimated owing to its being Compton-thick (see Subsection 4.2). [iii] Silicate absorption not detected. References for the X-ray luminosity: (a) Evans et al. (2006); (b) Hardcastle et al. (2006); (c) Katzin et al. 2012 (in preparation);(d) Evans et al. (private communication); (e) Evans et al. (2008a); (f) Hardcastle et al. (2009); (g) Evans et al. (2008b); (h) Hardcastle et al. (2009); (i) Young et al. (2002).

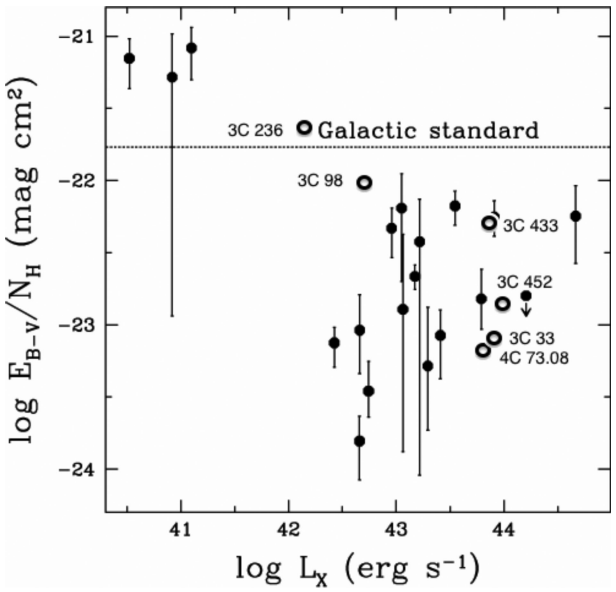

Figure 5. Dust-to-gas ratio comparison of AGNs (solid circles) and the Galactic ratio (dashed line) taken from Maiolino et al. (2001). Open circles represent objects in our complete sample, using A_V(NIR) from the near-IR SED estimation [$E(B-V) = A_V/3.1$]. Note how the AGNs have lower dust-to-gas ratios than the Galaxy, and how our *HST* sample follows this trend too (except for 3C 236).

Franceschini et al. (2005) compiled IRAC, MIPS (Multiband Imaging Photometer) and X-ray data for 143 radio galaxies within the *Spitzer* Wide-Area Infrared Extragalactic Survey (SWIRE). Of these, 19 sources are type 1 with available data in the four IRAC channels (3.6, 4.5, 5.8 and 8.0 μm). We fitted the mid-IR IRAC SEDs of the unabsorbed type 1 AGNs from the photometry given in Franceschini et al. (2005), obtaining a median power-law index of $\alpha_{\rm MIR\text{–}Ty1} = 0.97 \pm 0.13$. Note that this spectral index is the same as the spectral index estimated by Simpson & Rawlings (2000) for unobscured radio quasars at near-IR wavelengths ($\overline{\alpha}_{\rm QSO} = 0.97$).

After de-reddening the mid-IR spectral index to match with the mid-IR spectral index of unextinguished type 1 radio galaxies, the extinction in the K band (A_K) was calculated using the extinction curve for the mid-IR range (Indebetouw et al. 2005), and then the equivalent optical extinction (A_V) was calculated using $A_\lambda \propto \lambda^{-1.7}$ (Mathis 1990). The extinctions based on the mid-IR spectral index, A_V(MIR), are presented in column 8 of Table 8.

4.5 IRS spectra: silicate absorption features

IRS spectroscopic data were extracted from the *Spitzer* Science Centre (SSC) archive in order to measure the silicate 9.7-μm absorption feature. Silicate absorption/emission features are often detected at 9.7 and 18 μm in AGNs (Rieke & Low 1975; Hao et al. 2005; Shi et al. 2006), and are caused by the silicate–oxygen (Si-O) stretching and O-Si-O bending vibrational modes, respectively. From the IRS *Spitzer* data, we estimated the optical depth of the 9.7-μm silicate absorption feature, $\tau_{9.7}$, relative to the continuum.

We used two methods to measure the optical depth of the silicate absorption feature: Gaussian fitting, and use of PAHFIT (Smith et al. 2007). The Gaussian method does not fit the polycyclic aromatic hydrocarbon (PAH) features, which can potentially lead to a systematic overestimation of $\tau_{9.7}$ because such features flank the silicate feature. On the other hand, it has been found that in the case of PAHFIT, the silicate feature is potentially underestimated because PAHFIT always tends to fit PAH emission, even if the spectra do not

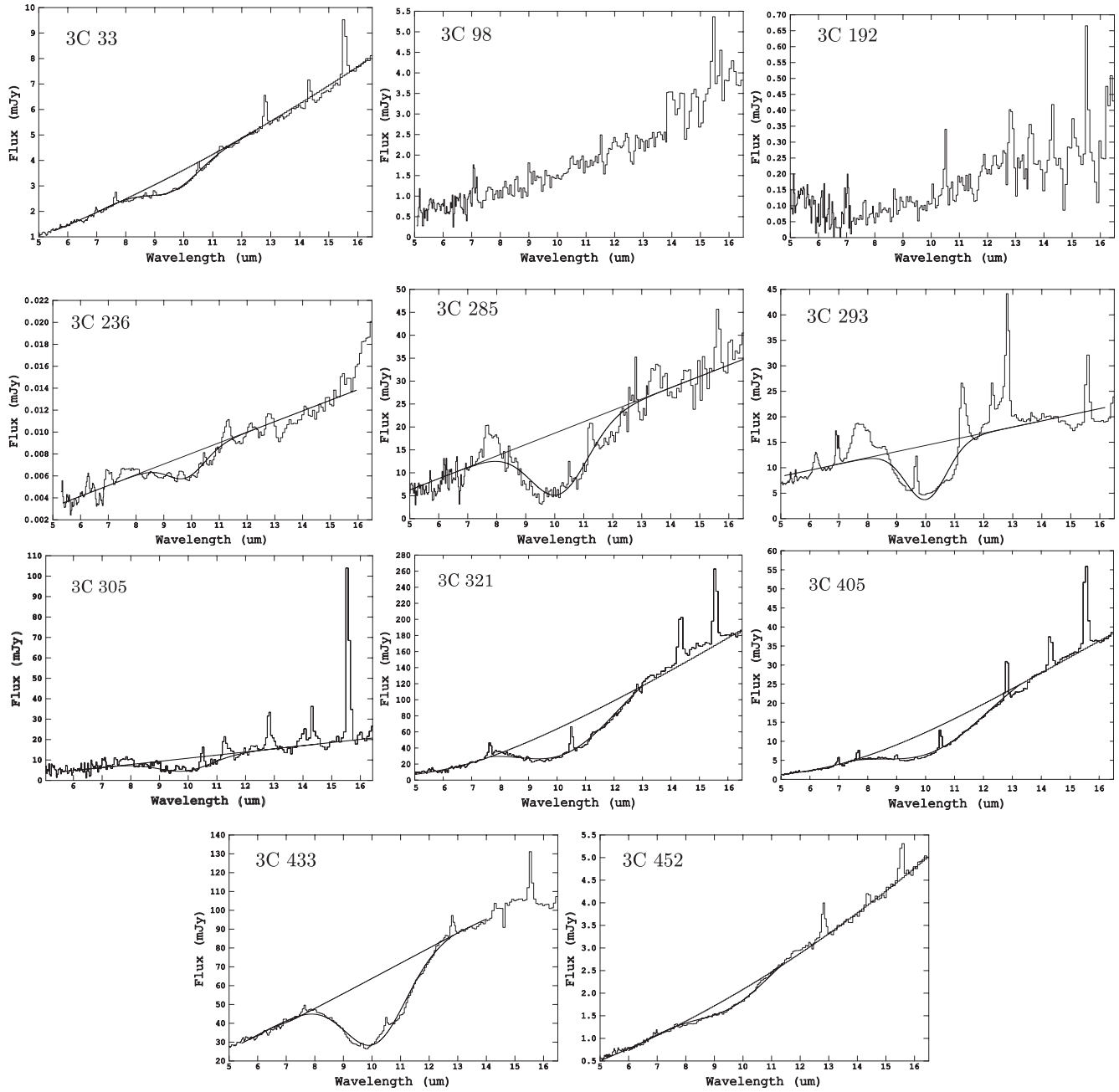

Figure 6. IRS spectra showing the Gaussian fits to the $\tau_{9.7}$ line and the spline fits to the continuum. The equivalent optical extinction was estimated using the relationship $A_V/\tau_{9.7} = 18.5 \pm 1$ (Whittet 1987).

show PAH emission lines. In consequence, the continuum will be lower and the silicate absorption depth lower. Because of this, we used the optical depths estimated by the Gaussian fitting method for the analysis in this study, and to estimate the optical extinctions. The method is described bellow.

We fitted a Gaussian profile to the silicate absorption feature using DIPSO, taking the regions with little PAH contamination on either side of the silicate absorption feature to estimate the continuum. Because of the more complex continuum shapes in the cases of 3C 321 and 3C 405, however, we fitted their continua using a spline line of order three. The spectra in Fig. 6 show the 9.7-μm silicate feature, together with the continuum and Gaussian fit. Note that no IRS data are available for 3C 277.3 and 4C 73.08.

The optical depth of the silicate line is

$$\tau_{9.7} = \log\left(\frac{F}{F_{\rm c}}\right), \qquad (2)$$

where F is the flux at the minimum of the Gaussian fit, and $F_{\rm c}$ is the interpolated flux of the continuum at the centre of the feature. The measured depths of the silicate absorption feature are presented in column 9 of Table 8. The uncertainties for the measured depths are estimated using the error in the 'peak' intensity of the fitted Gaussian. We then estimated A_V using the relationship $A_V/\tau_{9.7} = 18.5 \pm 1$ (Whittet 1987). Note that, even with the Gaussian method, care has been taken to account for potential PAH contamination, by the choice of appropriate continuum bins. The

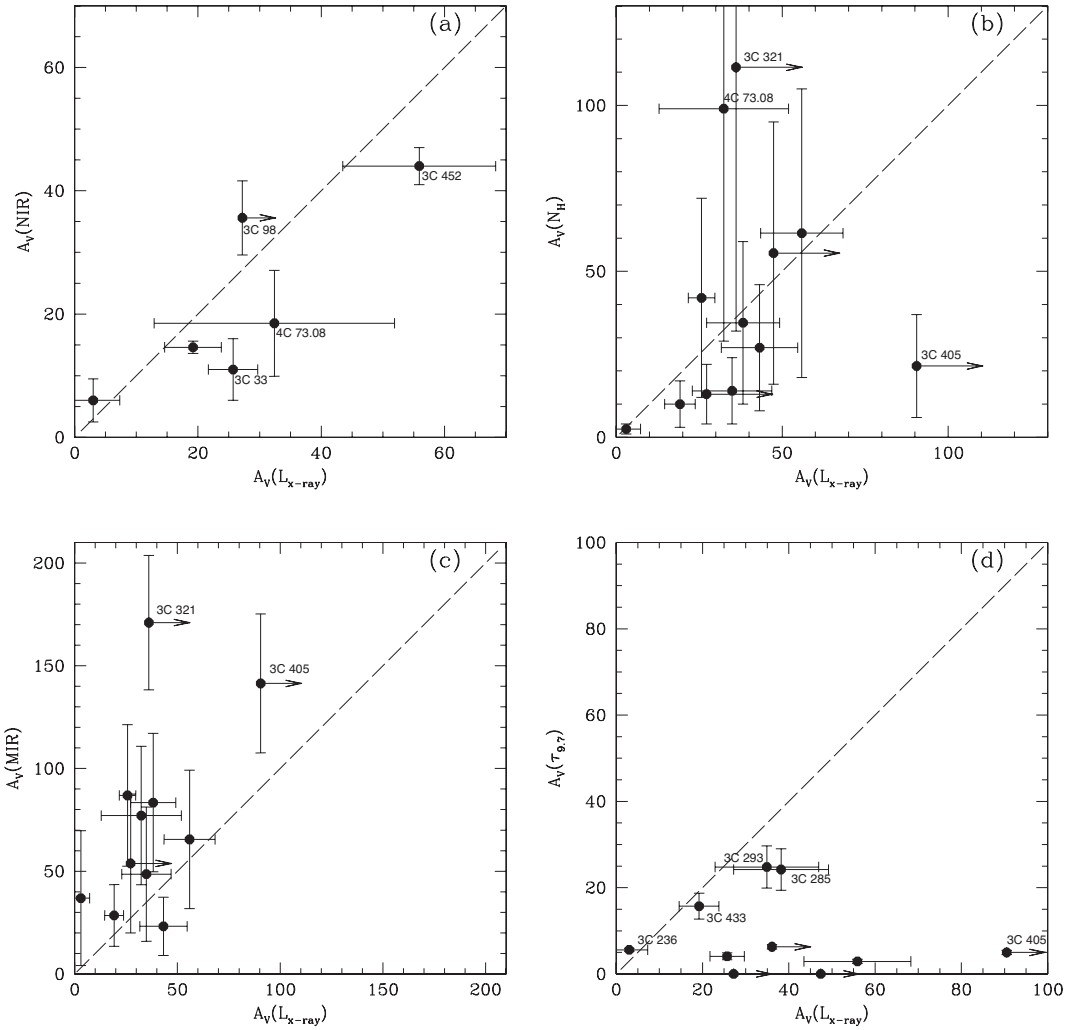

Figure 7. Comparisons of the extinctions estimated on the basis on the comparison between the X-ray luminosity and near-IR luminosity with extinctions estimated using: (a) the near-IR spectral index; (b) the X-ray column density after applying the correction of Maiolino et al. (2001); (c) the mid-IR spectral index; and (d) the silicate absorption feature optical depth ($\tau_{9.7}$ μm). Note that in the case of the extinction based on the silicate absorption feature ($\tau_{9.7}$, in (d)) the points cluster towards the bottom right-hand corner of the graph, indicating lower extinction compared with the estimates based on the X-ray/near-IR luminosity (and consequently the other methods).

extinctions based on the silicate feature, $A_V(\tau_{9.7})$, are presented in column 10 of Table 8.

5 DISCUSSION: COMPARISON OF THE EXTINCTION ESTIMATES

The estimates of the extinction of the nuclei derived using the five methods, namely from the near-IR spectral index, the X-ray/near-IR luminosity, the X-ray column density, the mid-IR spectral index, and based on the silicate spectral feature, are presented in Table 8. A comparison of these extinctions shows that in most objects the extinction based on the silicate optical depth is significantly lower than that obtained with the other techniques. Indeed, in some cases no silicate absorption is detected, but a large amount of extinction is estimated on the basis of the techniques involving near-IR, mid-IR and X-ray data (e.g. 3C 98).

Fig. 7 compares the extinction estimates derived from the various methods with the extinction based on the comparison of the X-ray luminosity and near-IR luminosity, $A_V(L_{\rm X\text{-}ray})$. As can be seen in Fig. 7(a), the extinctions based on the near-IR spectral index are similar to those based on the X-ray/near-IR luminosity. In the case of 3C 33, however, the extinction estimated on the basis of the near-IR spectral index is much lower than that estimated from its X-ray luminosity, by a factor of 0.4. On the other hand, although 4C 73.08 is located on the right-hand side of Fig. 7(a), the optical extinctions based on the two techniques agree within 1σ.

A comparison of the mean optical extinction based on the results of Maiolino et al. (2001) versus the extinction based on the X-ray/near-IR luminosity is shown in Fig. 7(b). Looking closely at this figure, it can be seen that the extinction for most of the sources (12 sources) is consistent with the extinction based on the X-ray/near-IR, except for three cases: 3C 321, 4C 73.08 and 3C 405.

Fig. 7(c) shows that the extinction based on the mid-IR spectral index is similar within 2σ (or slightly higher than) the extinction based on the X-ray/near-IR luminosity, except for 3C 321 and 3C 405. However, in these two latter cases the extinction based on the X-ray/near-IR luminosity, $A_V(L_{\rm X\text{-}ray})$, is a lower limit.

On the other hand, Fig. 7(d) shows that the extinction estimated by the silicate absorption feature tends to be on the bottom right-hand

side of the graph, far from the linear correlation (except for 3C 236, 3C 285, 3C 293 and 3C 433). This implies that in most objects the extinction based on the silicate optical depth is significantly lower than the extinction derived from the X-ray/near-IR luminosity, and consequently than that derived using the other four independent techniques. For instance, in 3C 98 and 3C 192 no silicate absorption is detected; however, a large amount of extinction is derived based on the other four independent techniques. Note that for 3C 305 the extinction based on the silicate optical depth is also lower than the extinction based on the mid-IR spectral index (see Table 8).

It is important to emphasize that the extinctions have been estimated under the assumption that the AGN is obscured by a foreground screen of dust (in this case the torus). Indeed, the Galactic $A_V/\tau_{9.7} = 18.5 \pm 1$ ratio (Whittet 1987), used to estimate the extinction based on the silicate absorption feature, assumes a point source absorbed by material in the foreground. That extinctions based on the silicate absorption feature are lower than the others indicates a departure from this simple model. Possible explanations include the following.

(i) Dilution by thermal mid-IR emission from the extended narrow-line region on a kiloparsec scale surrounding the AGN. Regardless of the scale of the torus, it is possible to have mid-IR radiation from dust outside the torus illuminated by the AGN. Indeed, it has been observed that mid-IR emission ($\sim$10μm) in many AGNs is extended, as for example in the case of Cygnus A (Radomski et al. 2002) and other objects (van der Wolk et al. 2010). Because this emission is on a larger scale, it will not be absorbed by the torus and will dilute the silicate absorption feature.

(ii) Dilution by non-thermal emission components from the jets. Synchrotron emission from radio core components on a larger scale than the torus will not suffer torus extinction and may dilute the silicate absorption feature.

(iii) Dilution by radiation from the illuminated faces of clouds in a clumpy torus. In a clumpy torus (Nenkova et al. 2002; Schartmann et al. 2008), some of the emission will escape directly from the torus, without suffering much extinction. This radiation will dilute the silicate absorption feature and lead to underestimation of the extinction.

At present, we cannot clearly distinguish among possibilities with the existing data. Clearly, further mid-IR observations with higher angular resolution will be required to separate the mid-IR emission of the torus from any extended mid-IR emission (Ramos Almeida et al. 2011). On the other hand, it has been suggested that the intrinsic SEDs of the synchrotron core sources might follow a power law that declines between the radio and the mid-IR wavelengths (Dicken et al. 2008), or have a parabolic shape (Landau et al. 1986; Leipski et al. 2009; van der Wolk et al. 2010). It is then necessary to examine the SEDs, including the radio core emission, to determine whether the silicate feature is contaminated by synchrotron emission. In addition, the clumpy torus model has to be applied to test whether the model reproduces the overall shape of the SEDs and the silicate feature.

6 CONCLUSIONS

In this paper we have presented deep *HST* near-IR imaging and *Spitzer* mid-IR photometric and spectroscopic data, which have been used to investigate the nature of the central obscuring regions in a sample of nearby 3C radio galaxies with FRII radio structures. The main results are as follows.

(i) Regarding the imaging analysis, we found that 80 per cent of the sources in our complete *HST* sample present an unresolved point source at 2.05 μm, and, in the extended sample of 13 sources, 77 per cent show an unresolved source, compared with 32 per cent in the optical *HST* study of Chiaberge et al. (2000). On the other hand, taking the shortest near-IR wavelength (1.025 μm), we find that only 30 per cent of the sources in our complete *HST* sample, and 25 per cent of the sources in the extended sample show an unresolved point source. In conclusion, the high point-source detection rate at near-IR wavelengths supports the idea that the overwhelming majority of NLRGs contain a hidden AGN in their centre, providing strong support for orientation-based unified schemes.

(ii) We find that the AGN is detected in 100 per cent of the sources at 8.0 μm in both our complete sample and the extended sample. At the shortest wavelength observed by IRAC (3.6 μm), the AGN component is detected in 25 per cent of the sources in our complete *HST* sample, and in 30 per cent of the sources in the extended sample with IRAC photometry. In conclusion, the 8.0-μm fluxes are dominated by the AGNs, while at 3.6 μm the stellar contribution makes AGN detection difficult at the low resolution of *Spitzer*. Detailed analysis of the *HST* and *Spitzer* images has shown an increasing number of core source detections towards longer wavelengths. This suggests a direct view of the AGN shining through a dusty torus, with the source more easily detected towards longer IR wavelengths. The detection rate of unresolved core sources suggests that the overwhelming majority of the NLRGs harbour an active nucleus.

(iii) We found that the radio-loud AGNs in our extended sample have a lower dust-to-gas ratio than the Galactic standard, consistent with the results of a sample of radio-quiet AGNs analysed by Maiolino et al. (2001). This implies that radio-loud and radio-quiet AGNs sublimate the dust near the nucleus more efficiently than in a normal galaxy such as the Milky Way.

(iv) The extinction imposed by the dust on an AGN has been estimated using five methods: using the near-IR spectral index, the X-ray/near-IR luminosity, the X-ray column density, the mid-IR spectral index, and based on the silicate spectral feature. In all cases the extinction was evaluated under the assumption that the dusty torus acts as a foreground screen that obscures the AGN. We found that the levels of extinction derived using the 9.7-μm silicate absorption feature are in general significantly lower than those estimated using the four other methods.

ACKNOWLEDGEMENTS

EAR is grateful for support from CONACyT and FAPESP. We would like to thank the anonymous referee for valuable comments and suggestions. This research has made use of the NASA/IPAC Extragalactic Database (NED) which is operated by the Jet Propulsion Laboratory, California Institute of Technology, under contract with the National Aeronautics and Space Administration. Based on observations made with the NASA/ESA *Hubble Space Telescope*, obtained from the data archive at the Space Telescope Science Institute. STScI is operated by the Association of Universities for Research in Astronomy, Inc. under NASA contract NAS 5-26555.

REFERENCES

Antonucci R., 1993, ARA&A, 31, 473
Baldi R. D. et al., 2010, ApJ, 725, 2426
Barthel P. D., 1989, ApJ, 336, 606
Bohlin R. C., Savage B. D., Drake J. F., 1978, ApJ, 224, 132

Buttiglione S., Capetti A., Celotti A., Axon D. J., Chiaberge M., Macchetto F. D., Sparks W. B., 2009, A&A, 495, 1033
Buttiglione S., Capetti A., Celotti A., Axon D. J., Chiaberge M., Macchetto F. D., Sparks W. B., 2010, A&A, 509, A6
Carilli C. L., Barthel P. D., 1996, A&AR, 7, 1
Chiaberge M., Capetti A., Celotti A., 2000, A&A, 355, 873
Chiaberge M., Capetti A., Celotti A., 2002, A&A, 394, 791
Demleitner M., Accomazzi A., Eichhorn G., Grant C. S., Kurtz M. J., Murray S. S., 2001, in Harnden F. R., Jr, Primini F. A., Payne H. E., eds, ASP Conf. Ser. Vol. 238, Astronomical Data Analysis Software and Systems X. Astron. Soc. Pac., San Francisco, p. 321
Dicken D., Tadhunter C., Morganti R., Buchanan C., Oosterloo T., Axon D., 2008, ApJ, 678, 712
Dicken D. et al., 2012, ApJ, 745, 172
Djorgovski S., Weir N., Matthews K., Graham J. R., 1991, ApJ, 372, L67
Draine B., 1989, Interstellar Dust, 135, 313
Evans D. A., Worrall D. M., Hardcastle M. J., Kraft R. P., Birkinshaw M., 2006, ApJ, 642, 96
Evans D. A. et al., 2008a, ApJ, 675, 1057
Evans D. A., Hardcastle M. J., Lee J. C., Kraft R. P., Worrall D. M., Birkinshaw M., Croston J. H., 2008b, ApJ, 688, 844
Fanaroff B. L., Riley J. M., 1974, MNRAS, 167, 31P
Franceschini A. et al., 2005, AJ, 129, 2074
Hao L. et al., 2005, ApJ, 625, L75
Hardcastle M. J., Evans D. A., Croston J. H., 2006, MNRAS, 370, 1893
Hardcastle M. J., Evans D. A., Croston J. H., 2009, MNRAS, 396, 1929
Indebetouw R. et al., 2005, ApJ, 619, 931
Kriss G. A., 1988, ApJ, 324, 809
Krist J., 2005, available at: http://irsa.ipac.caltech.edu/data/SPITZER/docs/dataanalysistools/tools/contributed/general/stinytim/
Krist J., Hook R., 2004, available at: http://www.stsci.edu/software/tinytim/
Laing R. A., Riley J. M., Longair M. S., 1983, MNRAS, 204, 151
Landau R. et al., 1986, ApJ, 308, 78
Leahy J. P., Bridle A. H., Strom R. G., 2000, An Atlas of DRAGNs. Jodrell Bank Obs., Macclesfield. Available at: http://www.jb.man.ac.uk/atlas/
Leipski C., Antonucci R., Ogle P., Whysong D., 2009, ApJ, 701, 891
Maccacaro T., Perola G. C., Elvis M., 1982, ApJ, 257, 47
Madrid J. P. et al., 2006, ApJS, 164, 307
Maiolino R., Marconi A., Salvati M., Risaliti G., Severgnini P., Oliva E., La Franca F., Vanzi L., 2001, A&A, 365, 28
Marchesini D., Capetti A., Celotti A., 2005, A&A, 433, 841
Mathis J. S., 1990, ARA&A, 28, 37
Mullin L. M., Riley J. M., Hardcastle M. J., 2008, MNRAS, 390, 595
Nenkova M., Ivezić Ž., Elitzur M., 2002, ApJ, 570, L9
Peng C. Y., Ho L. C., Impey C. D., Rix H.-W., 2002, AJ, 124, 266
Pier E. A., Krolik J. H., 1992, ApJ, 401, 99
Radomski J. T., Piña R. K., Packham C., Telesco C. M., Tadhunter C. N., 2002, ApJ, 566, 675
Ramírez E. A., Tadhunter C. N., Axon D., Batcheldor D., Young S., Packham C., Sparks W. B., 2009, MNRAS, 399, 2165
Ramos Almeida C. et al., 2011, ApJ, 731, 92
Ramos Almeida C. et al., 2012, MNRAS, 419, 687
Reichert G. A., Mushotzky R. F., Holt S. S., Petre R., 1985, ApJ, 296, 69
Rieke G. H., Low F. J., 1975, ApJ, 199, L13
Schartmann M., Meisenheimer K., Camenzind M., Wolf S., Tristram K. R. W., Henning T., 2008, A&A, 482, 67
Shi Y. et al., 2006, ApJ, 653, 127
Simpson C., Rawlings S., 2000, MNRAS, 317, 1023
Smith J. D. T. et al., 2007, ApJ, 656, 770
Spinrad H., Marr J., Aguilar L., Djorgovski S., 1985, PASP, 97, 932
Tadhunter C. N., Packham C., Axon D. J., Jackson N. J., Hough J. H., Robinson A., Young S., Sparks W., 1999, ApJ, 512, L91
Tadhunter C. N. et al., 2000, MNRAS, 313, L52
Temi P., Brighenti F., Mathews W. G., 2008, ApJ, 672, 244
Thatte D. et al., 2009, NICMOS Data Handbook. Baltimore: STScI, Version 8.0
Tody D., 1986, SPIE, 627, 733
Urry C. M., Padovani P., 1995, PASP, 107, 803
van der Wolk G., Barthel P. D., Peletier R. F., Pel J. W., 2010, A&A, 511, A64
Viana A. et al., 2009, NICMOS Instrument Handbook. Baltimore: STScI, Version 11.0
Whittet D. C. B., 1987, QJRAS, 28, 303
Wright E. L. et al., 2010, AJ, 140, 1868
Young A. J., Wilson A. S., Terashima Y., Arnaud K. A., Smith D. A., 2002, ApJ, 564, 176
Zirbel E. L., 1996, ApJ, 473, 713

This paper has been typeset from a TEX/LATEX file prepared by the author.